Electronic Supplementary Material (ESI) for Energy & Environmental Science.
This journal is © The Royal Society of Chemistry 2024

Supporting Information of

Entropy Engineering Enabled Atomically Dispersed Cu Doping Leading to Exceptionally High Thermoelectric Figure of Merit in n-type Lead Chalcogenides

Ziling Yuan[1,†], Mengyue Wu[1,†], Shuai Han[1,†], Pengfei Liu[4], Zhenhua Ge[5], Bangzhi Ge[1], Menghua Zhu[1], Yadong Xu[1], Wanqi Jie[1], Dongyao Zhao[6], Bingchao Yang[6], Yongsheng Zhang[6], Ming Liu[3], Min Zhu[7], Chao Li[2, *], Yuan Yu[3, *], Chongjian Zhou[1, *]

[1]*State Key Laboratory of Solidification Processing, and Key Laboratory of Radiation Detection Materials and Devices, Ministry of Industry and Information Technology, Northwestern Polytechnical University, Xi'an 710072, China*

[2]*The Fifth Electronics Research Institute of Ministry of Industry and Information Technology, Guangzhou 510006, China*

[3]*Institute of Physics (IA), RWTH Aachen University, 52056 Aachen, Germany*

[4]*Institute of High Energy Physics, Chinese Academy of Sciences, Beijing 100049, China Spallation Neutron Source Science Center, Dongguan 523803, China*

[5]*Faculty of Materials Science and Engineering, Kunming University of Science and Technology, Kunming, 650093, China*

[6]*Laboratory of High-Pressure Physics and Material Science (HPPMS), School of Physics and Physical Engineering, Qufu Normal University, Qufu, 273165, China*

[7]*State Key Laboratory of Functional Materials for Informatics, Shanghai Institute of Micro-System and Information Technology, Chinese Academy of Sciences; 200050 Shanghai, China*

[†]These authors contributed equally to this work

*Corresponding author. Email: cjzhou@nwpu.edu.cn, lichao@ceprei.com, yu@physik.rwth-aachen.de

Contents

1. Calculation Details

2. Table S1-S3

Table S1. The formation energies of all possible crystal structures by placing Cu atom over every interstitial site in matrix.

Table S2. The calculation of band gaps and electron effective mass for PbSe, $PbSe_{0.5}Te_{0.25}S_{0.25}$, $Pb_{0.99}Sn_{0.01}Se_{0.5}Te_{0.25}S_{0.25}$, $Cu_{0.004}PbSe$, $Cu_{0.004}Pb_{0.99}Sn_{0.01}Se$, $Cu_{0.004}PbSe_{0.5}Te_{0.25}S_{0.25}$, $Cu_{0.004}Pb_{0.99}Sn_{0.01}Se_{0.5}Te_{0.25}S_{0.25}$.

Table S3. The density of $Cu_{0.004}Pb_{1-x}Sn_xSe_{0.5}Te_{0.25}Se_{0.25}$ ($x = 0 – 0.1$).

3. Figures S1− S14

Figure S1. Energy dispersive spectrometer (EDS) image of the specimen. The corresponding EDS mappings of Cu, Pb, Sn, Se, Te and S revealing a homogeneous distribution of all elements.

Figure S2. Williamson-Hall plot for estimating microstrain (ε) of entropy-engineered lead chalcogenide $Cu_{0.004}Pb_{1-x}Sn_xSe_{0.5}Te_{0.25}S_{0.25}$ ($x = 0, 0.01, 0.05, 0.1$).

Figure S3. Microstructure characterization of $Cu_{0.004}PbSe_{0.5}Te_{0.25}S_{0.25}$ sample by transmission electron microscope (a) – (d) display representative low to high magnification images, demonstrating the presence of dense linear defects. The inset in (a) corresponds to the selected area diffraction pattern taken over the entire area, indicating the images are recorded along <110> zone axis.

Figure S4. Three-dimensional reconstruction of needle-shaped specimen. The orange, jasper, purple, green, yellow and wine dots correspond to the Cu, Pb, Se, Te, S and Sn atoms, respectively.

Figure S5. (a) Contour map of power factor as a function of temperature and hall carrier concentration (n_H). The colormap corresponds to changes in the *PF* value, with a trend towards yellow region indicating a higher *PF*. (b) The relationship between n_H and *PF*. The red line denotes the calculated optimized *PF* as a function of n_H based on single Kane band (SKB) model.

Figure S6. (a) Electrical conductivity and (b) Seebeck coefficient of $Pb_{0.9995}Sb_{0.0005}Se_{0.5}Te_{0.25}S_{0.25}$ and $Pb_{0.9885}Sn_{0.01}Sb_{0.0015}Se_{0.5}Te_{0.25}S_{0.25}$

Figure S7. Crystal structure of Cu doped $Pb_{0.99}Sn_{0.01}Se_{0.5}S_{0.25}Te_{0.25}$ systems with lowest formation energy.

Figure S8. The structure of $PbSe_{0.5}Te_{0.25}S_{0.25}$, $Pb_{0.99}Sn_{0.01}Se_{0.5}Te_{0.25}S_{0.25}$, $Cu_{0.004}PbSe$, $Cu_{0.004}Pb_{0.99}Sn_{0.01}Se$, $Cu_{0.004}PbSe_{0.5}Te_{0.25}S_{0.25}$ and $Cu_{0.004}Pb_{0.99}Sn_{0.01}Se_{0.5}Te_{0.25}S_{0.25}$.

Figure S9. Calculated Electronic Band structures for, $Cu_{0.004}PbSe$, $Cu_{0.004}Pb_{0.99}Sn_{0.01}Se$, $PbSe_{0.5}Te_{0.25}Se_{0.25}$, $Pb_{0.99}Sn_{0.01}Se_{0.5}Te_{0.25}Se_{0.25}$, The band gap and effective mass at the conduction band minimum (CBM) are extracted.

Figure S10. Experimentally measured room temperature lattice thermal conductivity (κ_{lat}) alongside transverse (v_t) and longitudinal (v_l) sound velocities of pristine PbSe and entropy-engineered samples of $Cu_{0.004}Pb_{1-x}Sn_xSe_{0.5}Te_{0.25}S_{0.25}$ ($x = 0, 0.01, 0.05, 0.1$)

Figure S11. Calculated phonon (a) band structure, (b) accumulated lattice thermal conductivity at 300 K and (c) temperature-dependent κ_{lat} of pristine PbSe and entropy-engineered $Pb_{0.99}Sn_{0.01}Se_{0.5}Te_{0.25}S_{0.25}$.

Figure S12. Comparisons of thermoelectric transport performance in n-type PbSe-based thermoelectric materials such as $Pb_{0.89}Sb_{0.012}Sn_{0.1}Se_{0.5}Te_{0.25}S_{0.25}$,[3] $Cu_{0.005}PbSe_{0.99}Te_{0.01}$,[4] $Pb_{1.075}Se_{0.8}Te_{0.2}$,[5] $Pb_{0.95}Sb_{0.033}Se_{0.6}Te_{0.4}$,[6] $Pb_{1.02}Se_{0.72}Te_{0.2}S_{0.08}$-0.3%Cu and $Pb_{0.9955}Sb_{0.0045}Se$-12%GeSe.[7,8] ZT_{ave} value at 300–573 K and 300–723K.

Figure S13. Thermoelectric properties of three independently synthesized $Cu_{0.004}Pb_{0.99}Sn_{0.01}Se_{0.5}Te_{0.25}Se_{0.25}$ entropy engineered samples. (a) ZT value, (b) power factor (*PF*), (c) electrical conductivity (σ), (d) Seebeck coefficient (*S*), (e) lattice thermal conductivity (κ_{lat}) and (f) total thermal conductivity (κ_{tot}).

Figure S14. Typical photographs of spark plasma sintered (SPS) high density specimens, which were cut and polished for thermoelectric property measurements. (a) The diameter and (b) height of typical SPS processed cylinder-shaped specimen. (c) Typical photograph of cut and polished SPS samples for measuring thermoelectric properties.

4. References

1. Calculation Details

Calculations for Pisarenko relation based on a single Kane band model (SKB).

Pisarenko relation is calculated employing a single Kane band model, assuming acoustic phonons dominate scattering mechanism. The carrier concentration (*n*), Seebeck coefficient (*S*), carrier mobility (μ), Lorenz number (*L*), electrical conductivity (σ), and power factor (*PF*) can be approximated by the equations (1) – (5):[1]

$$n = \frac{(2m^{*}k_{B}T)^{3/2}}{3\pi^{2}\hbar^{3}}\,{}^{0}F_{0}^{3/2} \tag{1}$$

$$S = \frac{k_{B}}{e}\left[\frac{{}^{1}F_{-2}^{1}}{{}^{0}F_{-2}^{1}} - \xi\right] \tag{2}$$

$$\mu = \frac{2\pi\hbar^{4}eC_{l}}{m_{I}^{*}(2m_{b}^{*}k_{B}T)^{3/2}\,\Xi^{2}}\,\frac{3\,{}^{1}F_{-2}^{1}}{{}^{0}F_{-2}^{1}} \tag{3}$$

$$L = \left(\frac{k_{B}}{e}\right)^{2}\left[\frac{{}^{2}F_{-2}^{1}}{{}^{0}F_{-2}^{1}} - \left(\frac{{}^{1}F_{-2}^{1}}{{}^{0}F_{-2}^{1}}\right)^{2}\right] \tag{4}$$

$${}^{n}F_{k}^{m} = \int_{0}^{\infty}\left(-\frac{\partial f}{\partial\varepsilon}\right)\varepsilon^{n}(\varepsilon+\alpha\varepsilon^{2})^{m}\left[(1+2\alpha\varepsilon)^{2}+2\right]^{k/2}d\varepsilon \tag{5}$$

In the equations, $\hbar$ is the reduced Planck constant, T is the absolute temperature, k_B is the Boltzmann constant, m^* is the density of states effective mass given band degeneracy, C_l (9.1 × 10^{10} Pa for PbSe) is a parameter determined by combining elastic constants,[2] *e* is the elementary positive charge, α is the reciprocal reduced band gap given by k_BT/E_g, in which E_g is the band gap. Ξ is the deformation potentials for multivalley systems, describing carrier scattering strength by acoustic phonons.

Table S1. The formation energies of all possible crystal structures by placing Cu atom over every interstitial site in matrix.

Config	$E_{\mathrm{formation}}$ (eV)	Config	$E_{\mathrm{formation}}$ (eV)	Config	$E_{\mathrm{formation}}$ (eV)	Config	$E_{\mathrm{formation}}$ (eV)
1	1.11	33	1.10	65	1.11	97	1.24
2	1.17	34	1.27	66	1.10	98	1.08
3	1.18	35	1.09	67	1.19	99	1.16
4	1.21	36	1.18	68	1.13	100	1.15
5	1.16	37	1.26	69	1.25	101	1.24
6	1.08	38	1.13	70	1.17	102	1.21
7	1.22	39	1.25	71	1.18	103	1.14
8	1.13	40	1.20	72	1.15	104	1.28
9	1.11	41	1.20	73	1.15	105	1.10
10	1.16	42	1.31	74	1.22	106	1.10
11	1.19	43	1.13	75	1.16	107	1.25
12	1.25	44	1.07	76	1.09	108	1.26
13	1.19	45	1.24	77	1.16	109	1.23
14	1.19	46	1.22	78	1.15	110	1.12
15	1.08	47	1.10	79	1.23	111	1.24
16	1.12	48	1.16	80	1.25	112	1.22
17	1.27	49	1.17	81	1.09	113	1.27
18	1.23	50	1.14	82	1.15	114	1.17
19	1.20	51	1.16	83	1.17	115	1.21
20	1.28	52	1.14	84	1.09	116	1.26
21	1.13	53	1.18	85	1.16	117	1.09
22	1.28	54	1.27	86	1.16	118	1.14
23	1.15	55	1.17	87	1.15	119	1.15
24	1.15	56	1.16	88	1.27	120	1.14
25	1.28	57	1.11	89	1.11	121	1.23
26	1.25	58	1.12	90	1.12	122	1.17
27	1.20	59	1.15	91	1.20	123	1.24
28	1.29	60	1.16	92	1.10	124	1.27
29	1.18	61	1.19	93	1.25	125	1.13
30	1.15	62	1.16	94	1.18	126	1.11
31	1.30	63	1.29	95	1.08	127	1.16
32	1.09	64	1.31	96	1.27	128	1.18

Table S2. The calculation of band gaps and electron effective mass for PbSe, $PbSe_{0.5}Te_{0.25}S_{0.25}$, $Pb_{0.99}Sn_{0.01}Se_{0.5}Te_{0.25}S_{0.25}$, $Cu_{0.004}PbSe$, $Cu_{0.004}Pb_{0.99}Sn_{0.01}Se$, $Cu_{0.004}PbSe_{0.5}Te_{0.25}S_{0.25}$, $Cu_{0.004}Pb_{0.99}Sn_{0.01}Se_{0.5}Te_{0.25}S_{0.25}$.

Configuration	E_g (eV)	m_0 (m_e)		
		Γ→X	**Γ→R**	Average
PbSe	0.448	0.142	0.124	0.133
$PbSe_{0.5}Te_{0.25}S_{0.25}$	0.327	0.160	0.152	0.156
$Pb_{0.99}Sn_{0.01}Se_{0.5}Te_{0.25}S_{0.25}$	0.205	0.160	0.153	0.1565
$Cu_{0.004}PbSe$	0.390	0.148	0.148	0.148
$Cu_{0.004}Pb_{0.99}Sn_{0.01}Se$	0.339	0.156	0.156	0.156
$Cu_{0.004}PbSe_{0.5}Te_{0.25}S_{0.25}$	0.311	0.175	0.160	0.1675
$Cu_{0.004}Pb_{0.99}Sn_{0.01}Se_{0.5}Te_{0.25}S_{0.25}$	0.199	0.155	0.154	0.1545

Table S3. The density of $Cu_{0.004}Pb_{1-x}Sn_xSe_{0.5}Te_{0.25}Se_{0.25}$ ($x = 0 – 0.1$)

Sample (Sn concentration)	Density (g/cm^3)
0	7.5827
0.01	7.5980
0.05	7.7263
0.1	7.8264

3. Figures S1− S14

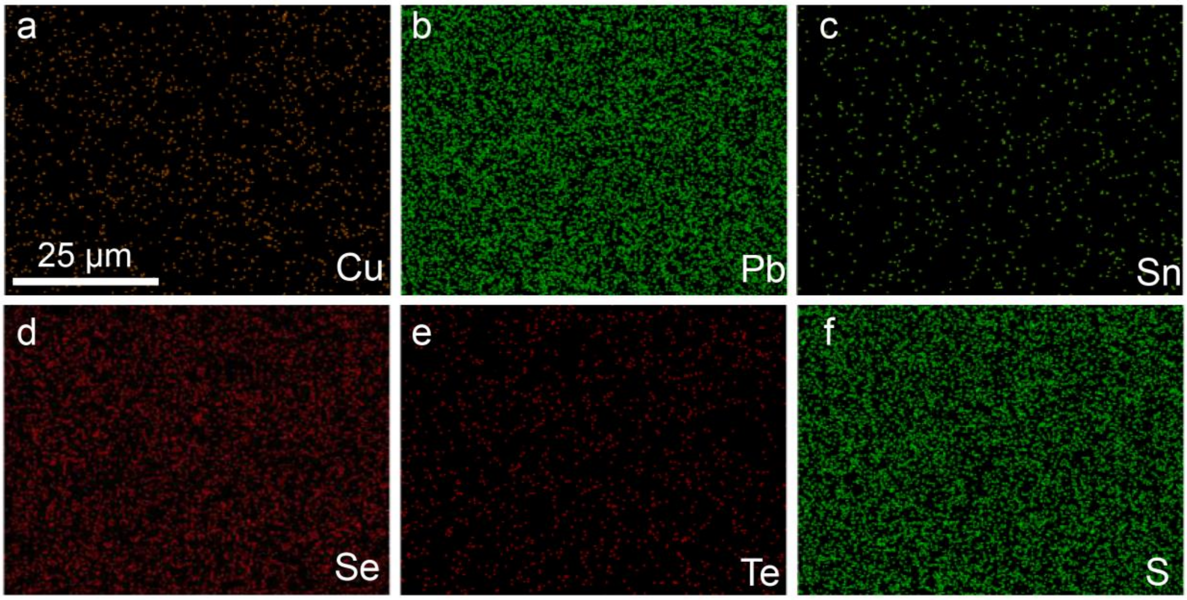

Figure S1. Energy dispersive spectrometer (EDS) image of the specimen. The corresponding EDS mappings of Cu, Pb, Sn, Se, Te and S revealing a homogeneous distribution of all elements.

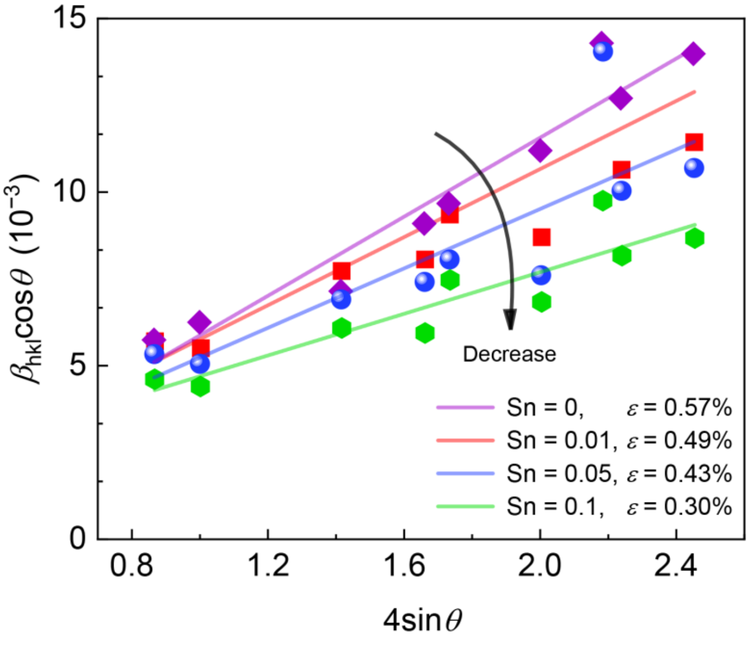

Figure S2. Williamson-Hall plot for estimating microstrain (ε) of entropy-engineered lead chalcogenide $Cu_{0.004}Pb_{1-x}Sn_xSe_{0.5}Te_{0.25}S_{0.25}$ (x = 0, 0.01, 0.05, 0.1).

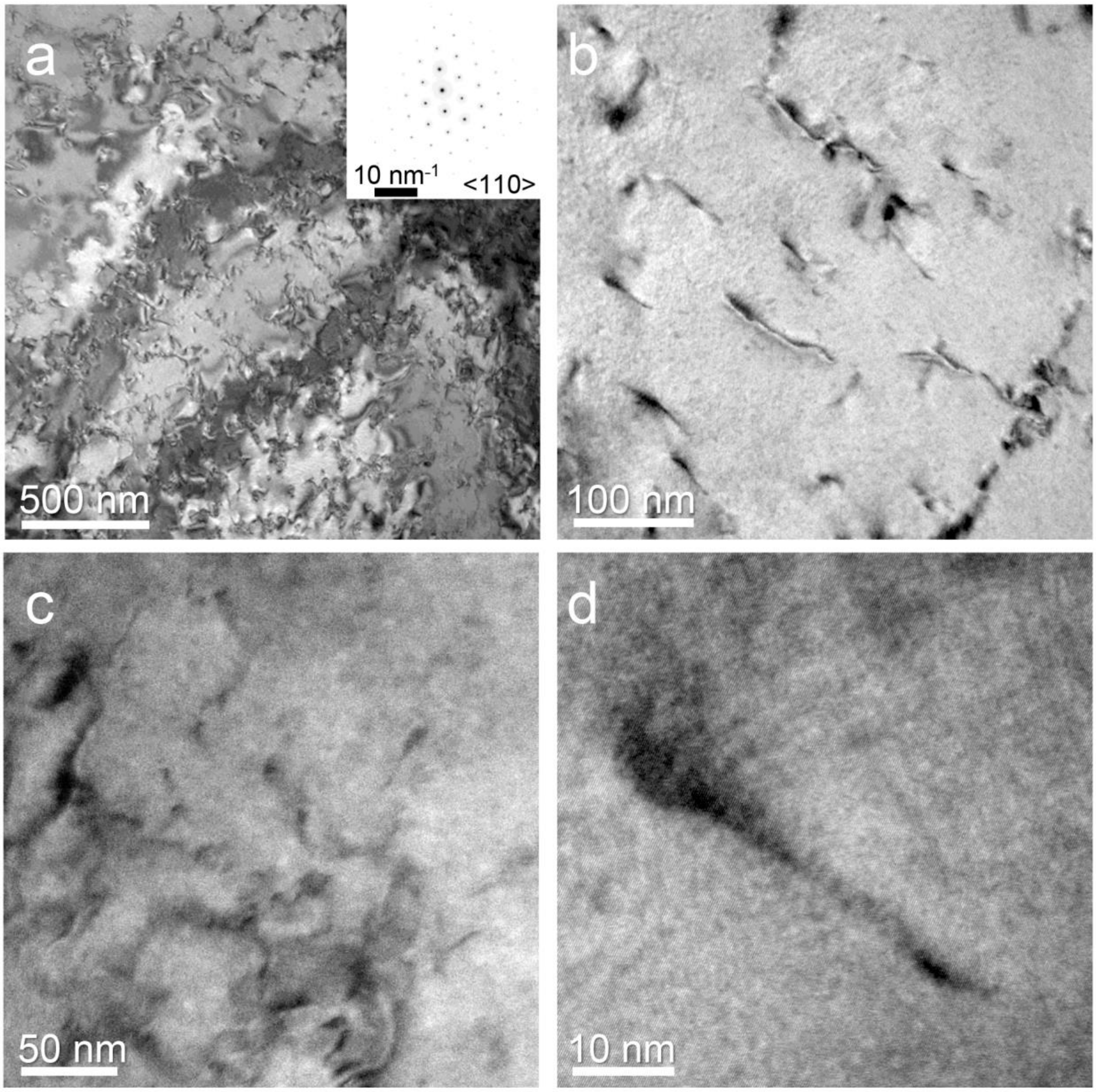

Figure S3. Microstructure characterization of $Cu_{0.004}PbSe_{0.5}Te_{0.25}S_{0.25}$ sample by transmission electron microscope (a) – (d) display representative low to high magnification images, demonstrating the presence of dense linear defects. The inset in (a) corresponds to the selected area diffraction pattern taken over the entire area, indicating the images are recorded along <110> zone axis.

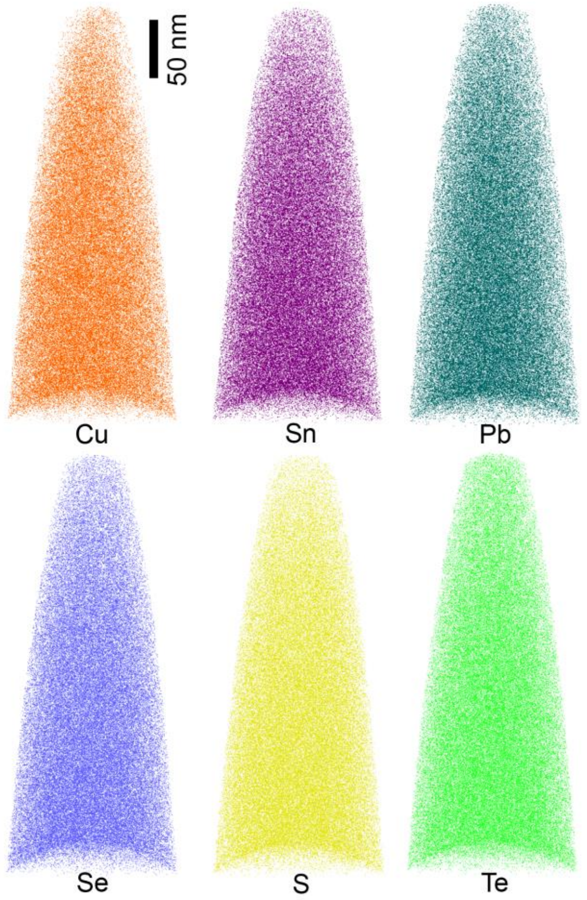

Figure S4. Three-dimensional reconstruction of needle-shaped specimen. The orange, jasper, purple, green, yellow and wine dots correspond to the Cu, Pb, Se, Te, S and Sn atoms, respectively.

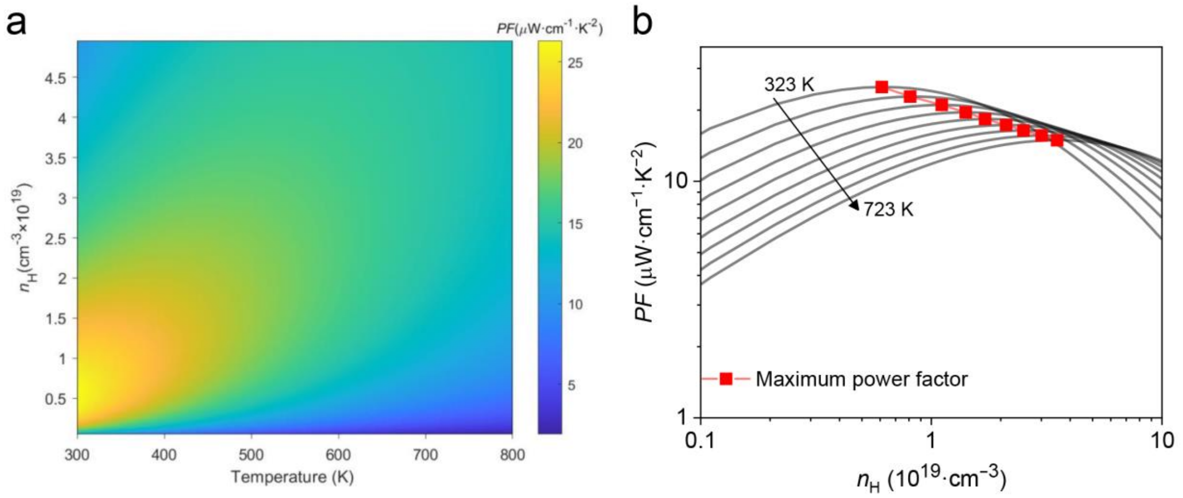

Figure S5. (a) Contour map of power factor as a function of temperature and hall carrier concentration (n_H). The colormap corresponds to changes in the *PF* value, with a trend towards yellow region indicating a higher *PF*. (b) The relationship between n_H and *PF*. The red line denotes the calculated optimized PF as a function of n_H based on single Kane band (SKB) model.

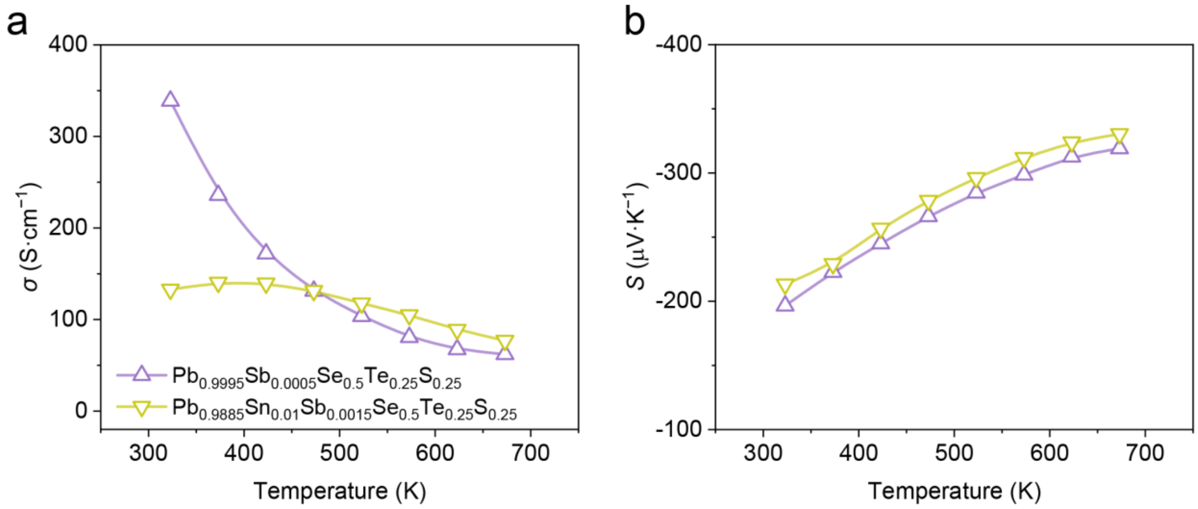

Figure S6. (a) Electrical conductivity and (b) Seebeck coefficient of $Pb_{0.9995}Sb_{0.0005}Se_{0.5}Te_{0.25}S_{0.25}$ and $Pb_{0.9885}Sn_{0.01}Sb_{0.0015}Se_{0.5}Te_{0.25}S_{0.25}$

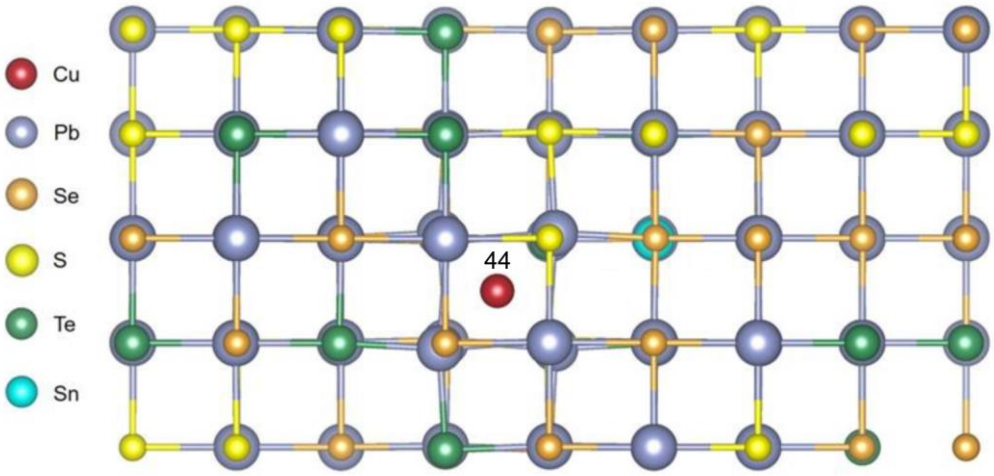

Figure S7. Crystal structure of Cu doped $Pb_{0.99}Sn_{0.01}Se_{0.5}S_{0.25}Te_{0.25}$ systems with lowest formation energy.

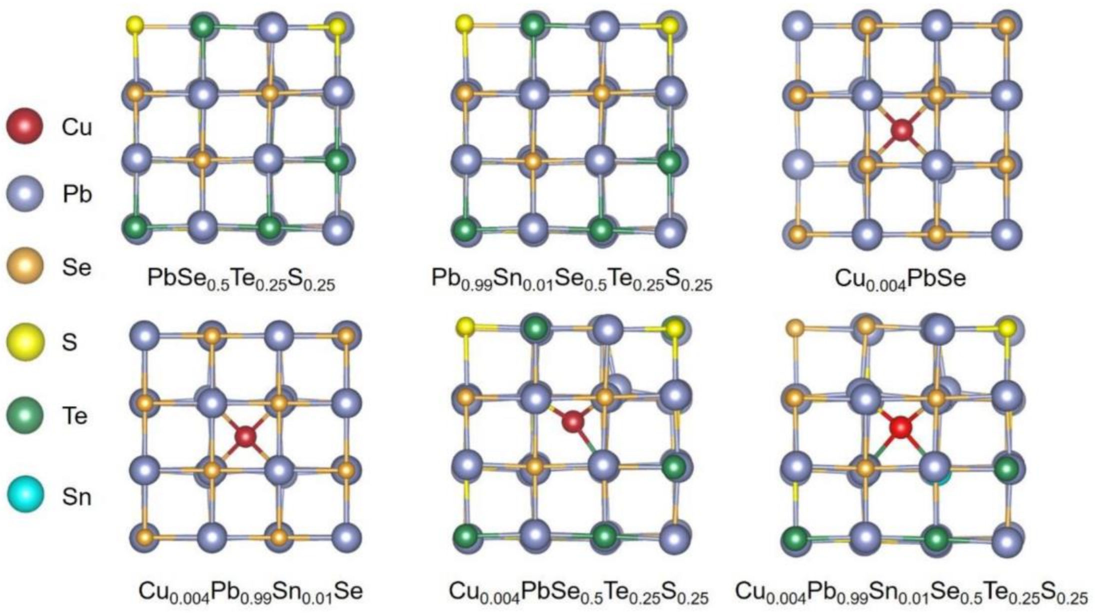

Figure S8. The structure of $PbSe_{0.5}Te_{0.25}S_{0.25}$, $Pb_{0.99}Sn_{0.01}Se_{0.5}Te_{0.25}S_{0.25}$, $Cu_{0.004}PbSe$, $Cu_{0.004}Pb_{0.99}Sn_{0.01}Se$, $Cu_{0.004}PbSe_{0.5}Te_{0.25}S_{0.25}$ and $Cu_{0.004}Pb_{0.99}Sn_{0.01}Se_{0.5}Te_{0.25}S_{0.25}$.

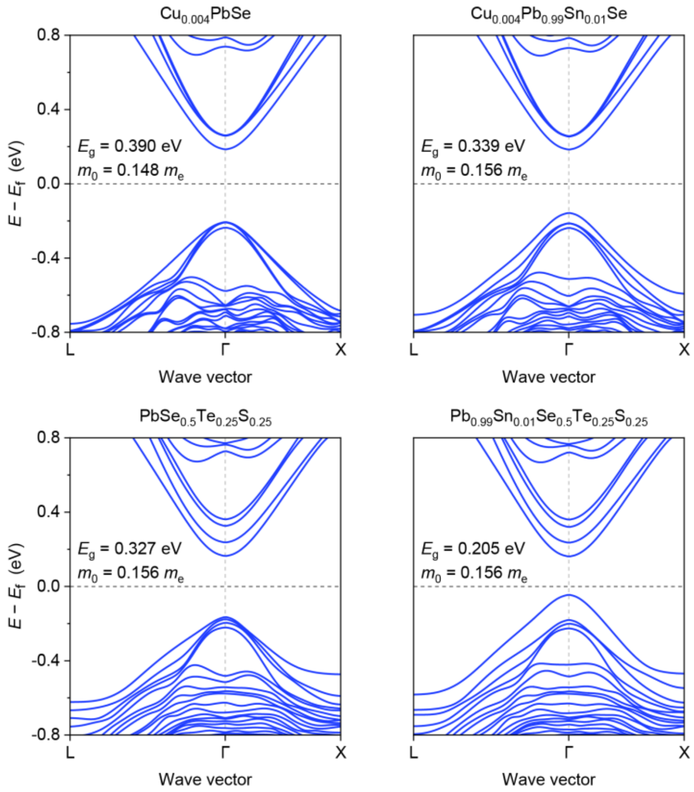

Figure S9. Calculated Electronic Band structures for, $Cu_{0.004}PbSe$, $Cu_{0.004}Pb_{0.99}Sn_{0.01}Se$, $PbSe_{0.5}Te_{0.25}Se_{0.25}$, $Pb_{0.99}Sn_{0.01}Se_{0.5}Te_{0.25}Se_{0.25}$, The band gap and effective mass at the conduction band minimum (CBM) are extracted.

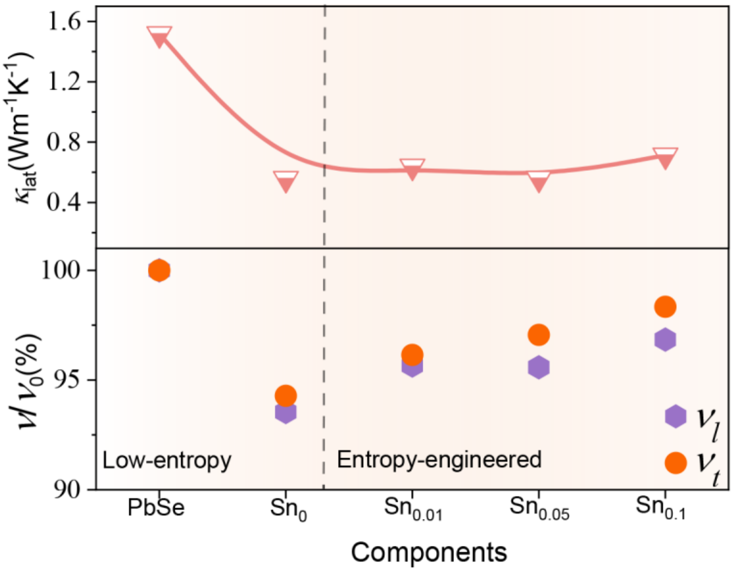

Figure S10. Experimentally measured room temperature lattice thermal conductivity (κ_{lat}) alongside transverse (v_t) and longitudinal (v_l) sound velocities of pristine PbSe and entropy-engineered samples of $Cu_{0.004}Pb_{1-x}Sn_xSe_{0.5}Te_{0.25}S_{0.25}$ (x = 0, 0.01, 0.05, 0.1)

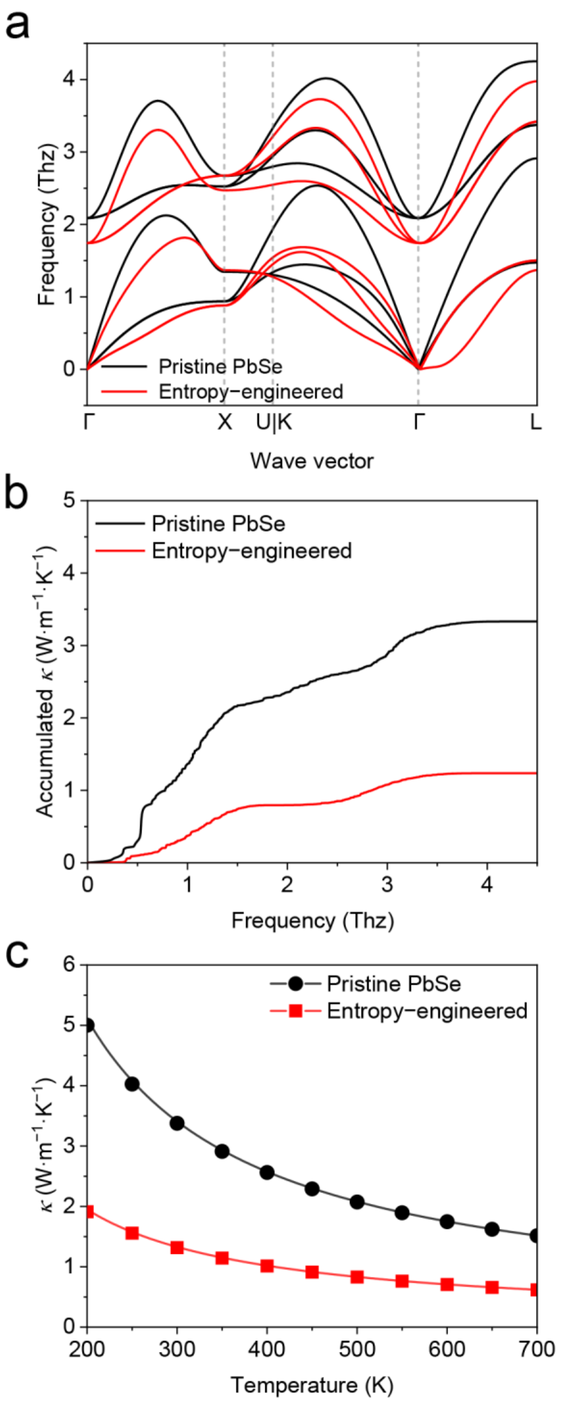

Figure S11. Calculated phonon (a) band structure, (b) accumulated lattice thermal conductivity at 300 K and (c) temperature-dependent κ_{lat} of pristine PbSe and entropy-engineered $Pb_{0.99}Sn_{0.01}Se_{0.5}Te_{0.25}S_{0.25}$.

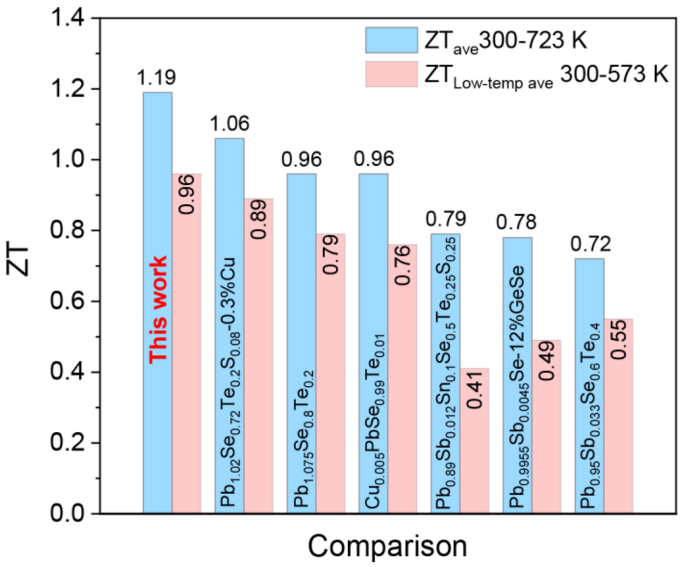

Figure S12. Comparisons of thermoelectric transport performance in n-type PbSe-based thermoelectric materials such as $Pb_{0.89}Sb_{0.012}Sn_{0.1}Se_{0.5}Te_{0.25}S_{0.25}$,[3] $Cu_{0.005}PbSe_{0.99}Te_{0.01}$,[4] $Pb_{1.075}Se_{0.8}Te_{0.2}$,[5] $Pb_{0.95}Sb_{0.033}Se_{0.6}Te_{0.4}$,[6] $Pb_{1.02}Se_{0.72}Te_{0.2}S_{0.08}$-0.3%Cu and $Pb_{0.9955}Sb_{0.0045}$Se-12%GeSe.[7,8] ZT_{ave} value at 300–573 K and 300–723K.

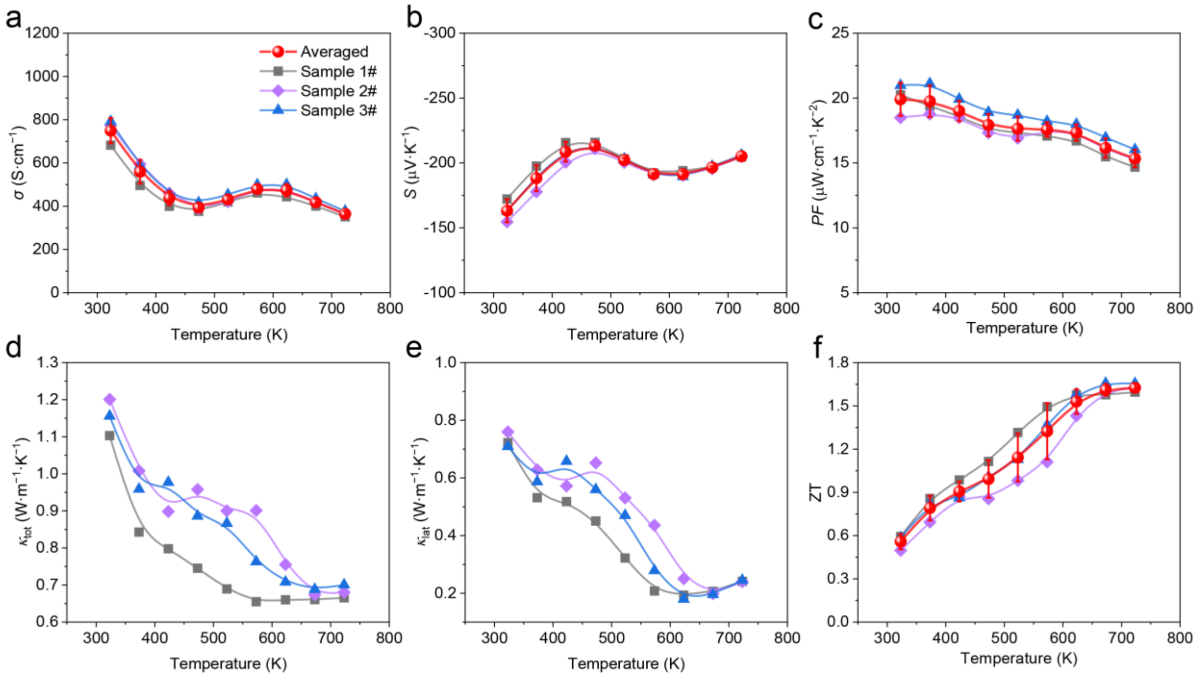

Figure S13. Thermoelectric properties of three independently synthesized $Cu_{0.004}Pb_{0.99}Sn_{0.01}Se_{0.5}Te_{0.25}Se_{0.25}$ entropy engineered samples. (a) ZT value, (b) power factor (*PF*), (c) electrical conductivity (σ), (d) Seebeck coefficient (S), (e) lattice thermal conductivity (κ_{lat}) and (f) total thermal conductivity (κ_{tot}).

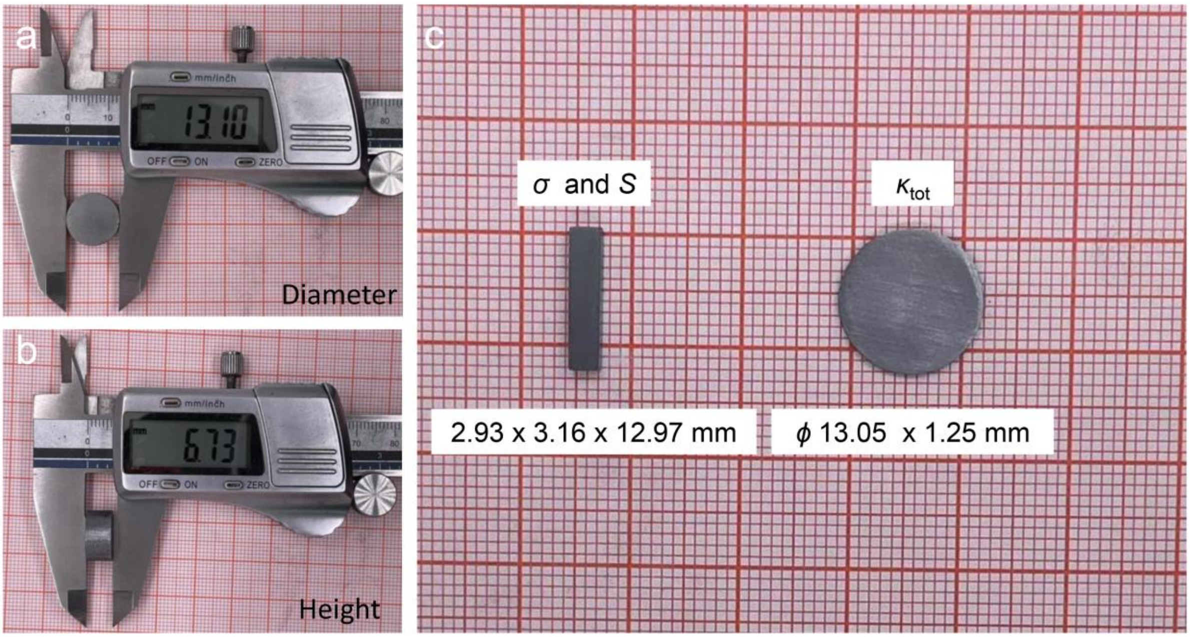

Figure S14. Typical photographs of spark plasma sintered (SPS) high density specimens, which were cut and polished for thermoelectric property measurements. (a) The diameter and (b) height of typical SPS processed cylinder-shaped specimen. (c) Typical photograph of cut and polished SPS samples for measuring thermoelectric properties.

4. References

1 Q. Zhang, Q. Song, X. Wang, J. Sun, Q. Zhu, K. Dahal, X. Lin, F. Cao, J. Zhou, S. Chen, G. Chen, J. Mao and Z. Ren, *Energy & Environmental Science*, 2018, **11**, 933-940.

2 H. Wang, Y. Pei, A. D. LaLonde and G. J. Snyder, *Proc Natl Acad Sci U S A*, 2012, **109**, 9705-9709.

3 B. Jiang, Y. Yu, J. Cui, X. Liu, L. Xie, J. Liao, Q. Zhang, Y. Huang, S. Ning, B. Jia, B. Zhu, S. Bai, L. Chen, S. J. Pennycook and J. He, *Science*, **2021**, 371, 830-834.

4 C. Zhou, Y. Yu, Y. L. Lee, B. Ge, W. Lu, O. Cojocaru-Miredin, J. Im, S. P. Cho, M. Wuttig, Z. Shi and I. Chung, *J. Am. Chem. Soc.*, **2020**, 142, 15172-15186.

5 B. Ge, H. Lee, L. Huang, C. Zhou, Z. Wei, B. Cai, S.-P. Cho, J.-F. Li, G. Qiao, X. Qin, Z. Shi and I. Chung, *Adv. Sci.*, **2022**, 9, e2203782.

6 C. Zhou, Y. K. Lee, J. Cha, B. Yoo, S. P. Cho, T. Hyeon and I. Chung, *J. Am. Chem. Soc.*, **2018**, 140, 9282-9290.

7 L. Xu, Y. Xiao, S. Wang, B. Cui, D. Wu, X. Ding and L. D. Zhao, *Nat. Commun.*, **2022**, 13, 6449.

8 Z. Luo, S. Hao, X. Zhang, X. Hua, S. Cai, G. Tan, T. P. Bailey, R. Ma, C. Uher, C. Wolverton, V. P. Dravid, Q. Yan and M. G. Kanatzidis, *Energy Environ. Sci.*, **2018**, 11, 3220-3230.